SHORT REPORT

An *in vitro* compartmental system underlines the contribution of mitochondrial immobility to the ATP supply in the NMJ

Topaz Altman[1], Danielle Geller[1,2], Elisabeth Kleeblatt[1], Tal Gradus-Perry[1] and Eran Perlson[1,2,*]

ABSTRACT

The neuromuscular junction (NMJ) is the largest, most-complex synapse in the human body. Motor neuron (MN) diseases, such as amyotrophic lateral sclerosis (ALS), specifically target MNs and the NMJs. However, little is known about the reasons for MN-selective neuronal and synaptic vulnerability in MN diseases. Here, utilizing a compartmental microfluidic *in vitro* co-culture system, we provide a possible explanation for why the NMJ, other than its unusual dimensions, differs from other synapses. By using live-imaging techniques, we discovered that cultured MNs display higher axonal and synaptic mitochondrial immobility compared with sympathetic neurons (SNs), leading to a profound enrichment of mitochondria only in the MN NMJ. Furthermore, by employing a synaptic ATP sensor, we show that mitochondrial respiration is the key contributor to ATP production in MN NMJs but not in SN synapses. Taken together, our data suggest that mitochondrial localization underlies the unique and specific qualities of MN NMJs. Our findings shed light on the role of mitochondria in MN and NMJ maintenance, and possibly indicate how mitochondria may serve as a source for selective MN vulnerability in neurodegenerative diseases.

This article has an associated First Person interview with the first author of the paper.

KEY WORDS: Axonal transport, Mitochondria, Neuromuscular junction, Motor neuron, Sympathetic neuron, Synaptic ATP

INTRODUCTION

Motor neurons (MNs) are large polarized cells, extending their axons to distances of over 1 m long in adult humans. MNs large cell bodies ($\sim$20–40 µm) are not profoundly different from cell bodies of other central nervous system (CNS) neurons (Burke et al., 1977), and axons of comparable lengths can be found in other peripheral nervous system (PNS) neurons (e.g. sensory, sympathetic and para-sympathetic) (Catala and Kubis, 2013). Another key feature of MNs is their neuromuscular junction (NMJ), a highly specialized and massive synapse. Unlike other neuronal synapses, which have an average size of 1 µm (Gylys et al., 2004), the MN NMJ is several orders of magnitude larger, usually 10–30 µm (Jones et al., 2017). Furthermore, the vast size of the NMJ compartment is not only a matter of individual synapse diameter; it is also affected by the number of NMJs per single axon (i.e. motor unit), which

[1]Department of Physiology and Pharmacology, Sackler Faculty of Medicine, Tel Aviv University, Ramat Aviv 69978, Tel Aviv, Israel. [2]Sagol School of Neuroscience, Tel Aviv University, Ramat Aviv 69978, Tel Aviv, Israel.

*Author for correspondence (eranpe@tauex.tau.ac.il)

E.K., 0000-0003-2517-9089; E.P., 0000-0001-6047-9613

can be up to 2000 synapses in a single motor unit (Burke and Tsairis, 1973).

The size and quantity of MN synapses pose an extreme metabolic challenge, since many cellular processes, such as synaptic release and Ca^{2+} buffering, require large quantities of ATP (Harris et al., 2012). A possible explanation for this is the number of mitochondria found in the NMJ, which is far greater than in any other synapse in the body (Misgeld et al., 2007; Misgeld and Schwarz, 2017). Mitochondria are known to play a key role in axonal metabolism (Saab et al., 2016) and in synaptic function, for their ability to buffer Ca^{2+} and provide ATP (Devine and Kittler, 2018). However, more than half of CNS synapses lack mitochondria (Shepherd and Harris, 1998), suggesting that, in the CNS, synaptic mitochondria play a more regulatory role (Cserép et al., 2018; Styr et al., 2019), rather than one involving stability and maintenance. This notion is strengthened by recent evidence supporting differential mitochondrial populations among various neuronal subtypes (Fecher et al., 2019). On the other hand, MN mitochondria are present in every NMJ, and cover almost all of the synaptic surface of the NMJ (Lee and Peng, 2006; Misgeld et al., 2007). Although the anatomic uniqueness of the MN and NMJs are well established, little is known about the physiological importance of NMJ mitochondrial enrichment.

To study the specific contribution of mitochondria to the NMJ, we characterize the mitochondria transport and ATP production-utilizing compartmental MN–muscle co-culture system we recently developed (Zahavi et al., 2015; Ionescu et al., 2016), and compare it to a sympathetic neuron (SN)–cardiomyocyte platform. SNs have long axonal processes and a specialized, yet different, distal synapse (Catala and Kubis, 2013), and are relatively unaltered in MN diseases (Piccione et al., 2015). Our data indicates lower mitochondrial mobility in MNs compared with SNs, followed by mitochondria accumulation only in the MN NMJ and not in the SN synapse. Furthermore, we show that inhibition of mitochondrial respiration alone reduces synaptic ATP levels to a minimum in MN NMJs. In SN synapses, both mitochondria and glycolysis dependency are observed, thus demonstrating that synaptic ATP production has higher dependency on mitochondria in the NMJ than the SN synapse. Taken together, our findings suggest that mitochondria play a major role in the function and maintenance of NMJs compared to other synapses, notably the SN synapse.

RESULTS AND DISCUSSION
Co-culture of MNs with skeletal muscle, and SNs with cardiomyocytes generates functional synapses *in vitro*

To study the properties of MN NMJs *in vitro*, we used microfluidic compartmental chambers (MFCs) (Ionescu et al., 2016). Briefly, primary mouse myoblasts and mouse ventral spinal cord explants (representing MNs) were plated in the distal and proximal compartments of the MFC, respectively (Fig. 1A). A similar method was used for co-culturing primary mouse cardiomyocytes with primary superior cervical ganglion explants (representing SNs)
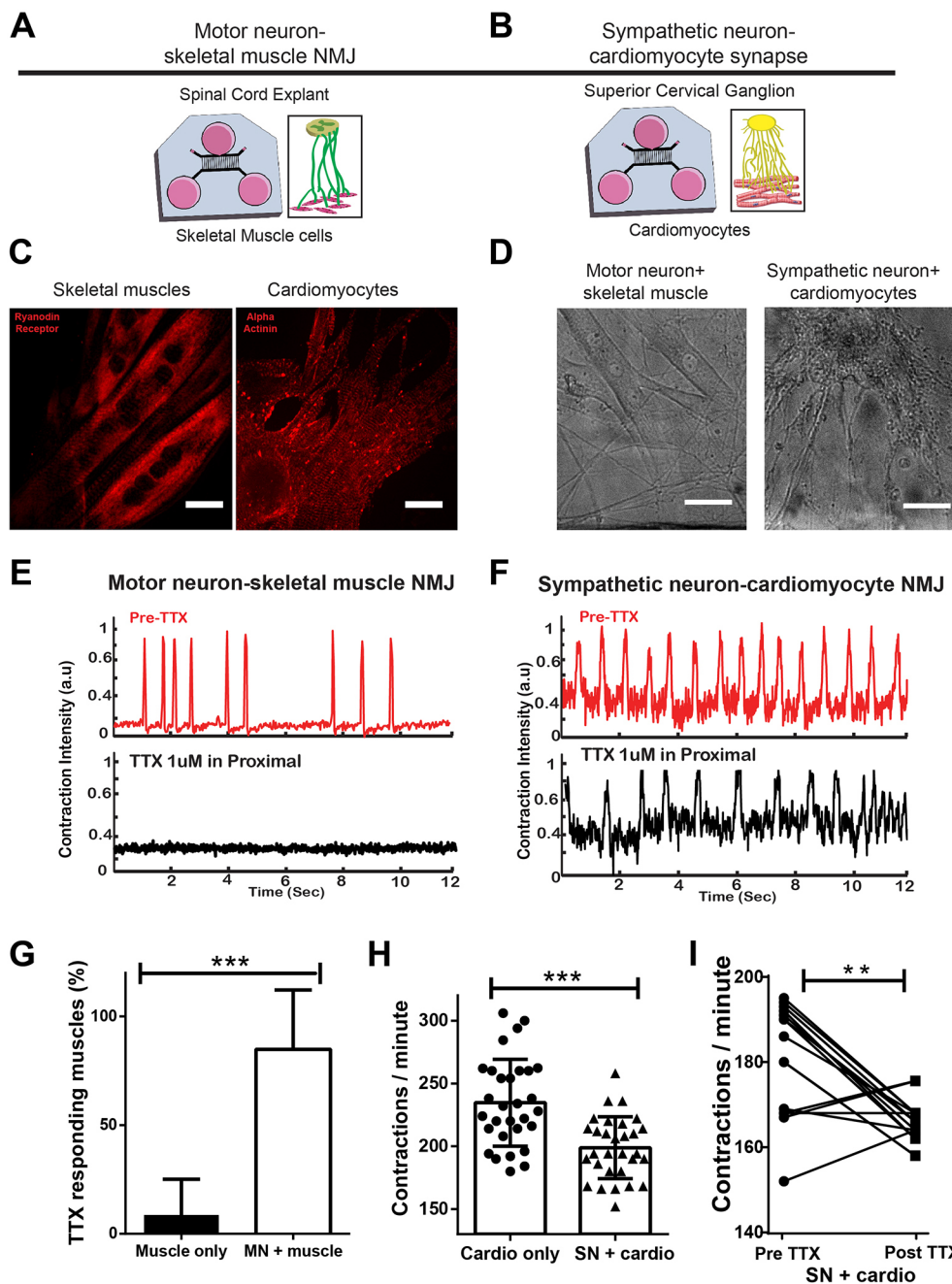
Fig. 1. An *in vitro* compartmental MFC as a platform for studying neuromuscular and sympathetic synapses. (A,B) Schematic illustration of the co-culture system, with ventral SC explants (representing MNs) and primary skeletal muscle cells (A) or superior cervical ganglions (representing SNs) and primary cardiomyocytes (B). (C) Immunofluorescence staining of matured skeletal muscles (RYR, left) or cardiomyocytes (α-actinin, right). Scale bars: 10 µm. (D) Phase-contrast image of skeletal muscle–MN (left) or cardiomyocyte–SN (right) co-culture. Scale bars: 20 µm. (E,F) Contraction graph displaying short bursts of contraction present in MN–skeletal muscle co-cultures (E), which were abolished after application of 1 µM TTX, or rhythmic cardiomyocyte contraction in SN–cardiomyocyte co-cultures (F), which was slowed down after applying 1 µM TTX. (G) The percentage of muscles responding to TTX was determined in the muscle-only condition (*n*=15 imaged fields) and for MN–skeletal muscle co-culture (*n*=17 imaged fields). ***$P<0.001$, Mann–Whitney test. (H) Average cardiomyocyte contraction rate with and without SNs; *n*=30 analyzed cardiomyocytes for both conditions. ***$P<0.001$, unpaired *t*-test. (I) Cardiomyocyte contraction rate before and after 1 µM TTX application; *n*=16 analyzed cardiomyocytes. **$P<0.01$, paired *t*-test. Each graph contains results from at least three independent biological repeats. Data represent mean±s.d. a.u., arbitrary units.

(Fig. 1B). The myoblasts and cardiomyocytes were differentiated into mature, fused muscles (Fig. 1C), and neurons crossed distally (Fig. 1D) to generate synapsin1-positive puncta (Fig. S1). Although the two systems were similar in many aspects, muscle function was distinctively different, as expected. MN presence generated sharp bursts of skeletal muscle contractions (Movie 1) that were abolished by MN application of 1 µM tetrodotoxin (TTX) (Fig. 1E). This did not occur, however, when TTX was applied onto muscle-only culture (Fig. 1G). Cardiomyocyte contraction was different, a repetitive rhythmic contraction (Fig. 1F; Movie 2) that was surprisingly impeded when SNs were present (Fig. 1H). This can be explained by an enhanced maturation process that changed the culture 'pacemaker' (Conforti et al., 1991; Oh et al., 2016). SN presence especially affected a specific subpopulation of cardiomyocytes, those with a slow pace baseline of under

200 beats/min. Following TTX application to SNs, only the slow subpopulation responded, and the number of contractions was significantly impeded (Fig. 1I). Taken together, we established these co-culture systems to study the MN versus SN synaptic unit.

Increased anterograde velocity and decreased retrograde transport in MN compared to SN

Numerous studies have shown alterations in axonal transport in MN diseases in general (Collard et al., 1995; Hafezparast et al., 2003; Münch et al., 2004; Bilsland et al., 2010; Gibbs et al., 2018), and specifically regarding mitochondrial transport (Magrané et al., 2014), but with no explanation of the specific vulnerability of MNs to those alterations. Importantly, SNs are relatively unaltered in MN diseases (Piccione et al., 2015). To this end, we chose to compare the basic qualities of mitochondrial transport in MNs and in SNs.

We plated spinal cord explants (MNs), superior cervical ganglions (SNs) or dorsal root ganglions (sensory neurons) in a compartmental system, extended their axons through microgrooves distally, and tracked axonal mitochondrial transport by using Mitotracker dye (Fig. 2A,B). Interestingly, MN axonal mitochondria displayed higher immobility compared with those of SNs or sensory neurons (Fig. 2C). The difference originated from lower retrograde transport in MN;

however, there was no difference in anterograde transport. To validate this finding, and to test the effect of synapse formation on mitochondrial transport, we repeated the experiment using a co-culture system for MNs or SNs. Even after synapses were formed, there were more non-motile MN mitochondria compared with SN mitochondria. The difference was mostly due to a lower rate of retrograde transport. To further characterize the properties of
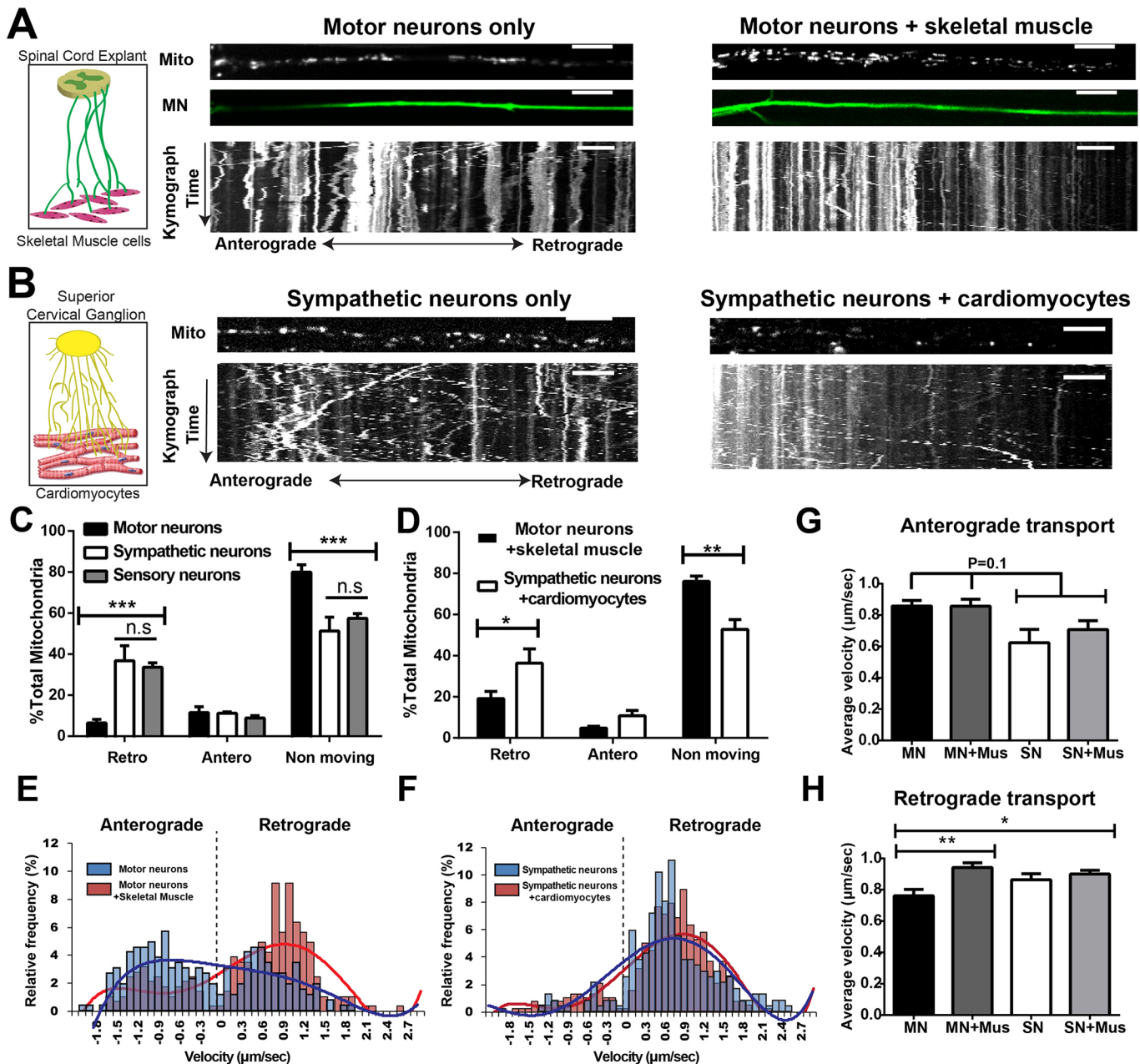
Fig. 2. MNs display decreased mitochondrial transport. (A,B) Representative axons and kymographs of MN-only culture (MN marker HB9::GFP) and MN–skeletal muscle co-culture (MN marker Chat::Rosa^{tdTomato}) (A) or SN-only culture and SN–cardiomyocyte co-culture (B). Mitochondria were stained with Mitotracker. Scale bar: 10 µm. Time of kymographs was 300 s. (C) Mitochondrial transport of MN-only culture compared with SN-only culture. n=5 MFCs per condition, at least 10 axons per MFC. ***P<0.001, two-way ANOVA with Holm–Sidak post-hoc test. (D) Mitochondrial transport of MN–skeletal muscle co-culture compared to SN–cardiomyocyte co-culture. n=4 MFCs for MN-skeletal muscles, n=5 for SN-cardiomyocytes, at least 10 axons per MFC. **P<0.01, *P<0.05, two-way ANOVA with Holm–Sidak post-hoc test. (E,F) Relative mitochondrial velocities distribution of MN-only culture or MN–skeletal muscle co-culture (E) and SN-only culture or SN-cardiomyocytes co-culture (F). (G,H) Average anterograde (G) and retrograde (H) transport of MNs and SNs with or without muscles. For G, P=0.1 for both comparisons, one-way ANOVA with Holm–Sidak post-hoc test. For H, **P<0.01, *P<0.05, one-way ANOVA with Holm–Sidak post-hoc test. For velocity analysis, n=254 moving mitochondria (147 anterograde, 107 retrograde) in MNs only, n=284 (76,208) in MNs plus skeletal muscles, n=236 (21,215) in SNs only and n=379 (57,322) in SNs plus cardiomyocytes. Each graph contains results from at least three independent biological repeats. Data represent mean±s.e.m.

mitochondrial axonal transport, we performed a thorough kinetic analysis of moving mitochondria (Fig. 2E,F). Our analysis revealed that MNs, both with and without presence of muscle, exhibit slightly (although not significantly) higher, anterograde velocity compared with SNs (Fig. 2G). Those differences between the two neuronal subtypes (the decreased retrograde transport and increased anterograde velocity) can be interpreted as a tendency of MN mitochondria to accumulate distally in order to support the NMJ mitochondrial-enriched synaptic structure, but may cause a lower mitochondrial recovery rate in cases of distal axonal stress.

Skeletal muscle affects MN mitochondrial axonal transport

The unique co-culture system allowed us to investigate the properties of mitochondrial axonal transport with muscle cell presence. Interestingly, the distribution of moving mitochondria velocities (Fig. 2E,F) was strongly influenced by skeletal muscle for MN mitochondrial axonal transport. The presence of skeletal muscle led to both an increased proportion of MN mitochondria undergoing retrograde transport (Fig. 2C,D) and to increased retrograde velocity (Fig. 2H). In the anterograde direction, there was an apparent shift in the proportion (Fig. 2C,D) but not in velocity (Fig. 2G) of mitochondria. However, those changes were not consistent with those seen for SNs and cardiomyocytes. Cardiomyocytes did not significantly change SN mitochondrial transport regarding either the proportion of mitochondria traveling in a particular direction (Fig. 2C,D) or their velocity (Fig. 2G,H). To better understand whether those changes were derived from muscle-secreted factors, we imaged axonal transport before and 3 h after applying muscle conditioned medium to the axonal compartment. Since this addition did not cause any change in axonal transport (Fig. S2), we investigated whether a change in MN transport was associated with NMJ formation. To this end, we compared mitochondrial axonal transport in the MN–muscle co-culture at three time points after axon cross: 5, 7 and 9 days in vitro (DIV), which represent the course of NMJ maturation. Interestingly, transport was consistently tilted toward the retrograde direction, with some changes during this time course (Fig. S3). Thus, we cannot rule out the possibility that muscle-secreted factors regulate MN axonal transport together with the formation of the NMJ. It is possible that only a continuous muscle secretion of factors can create a high local concentration gradient that facilitates this change.

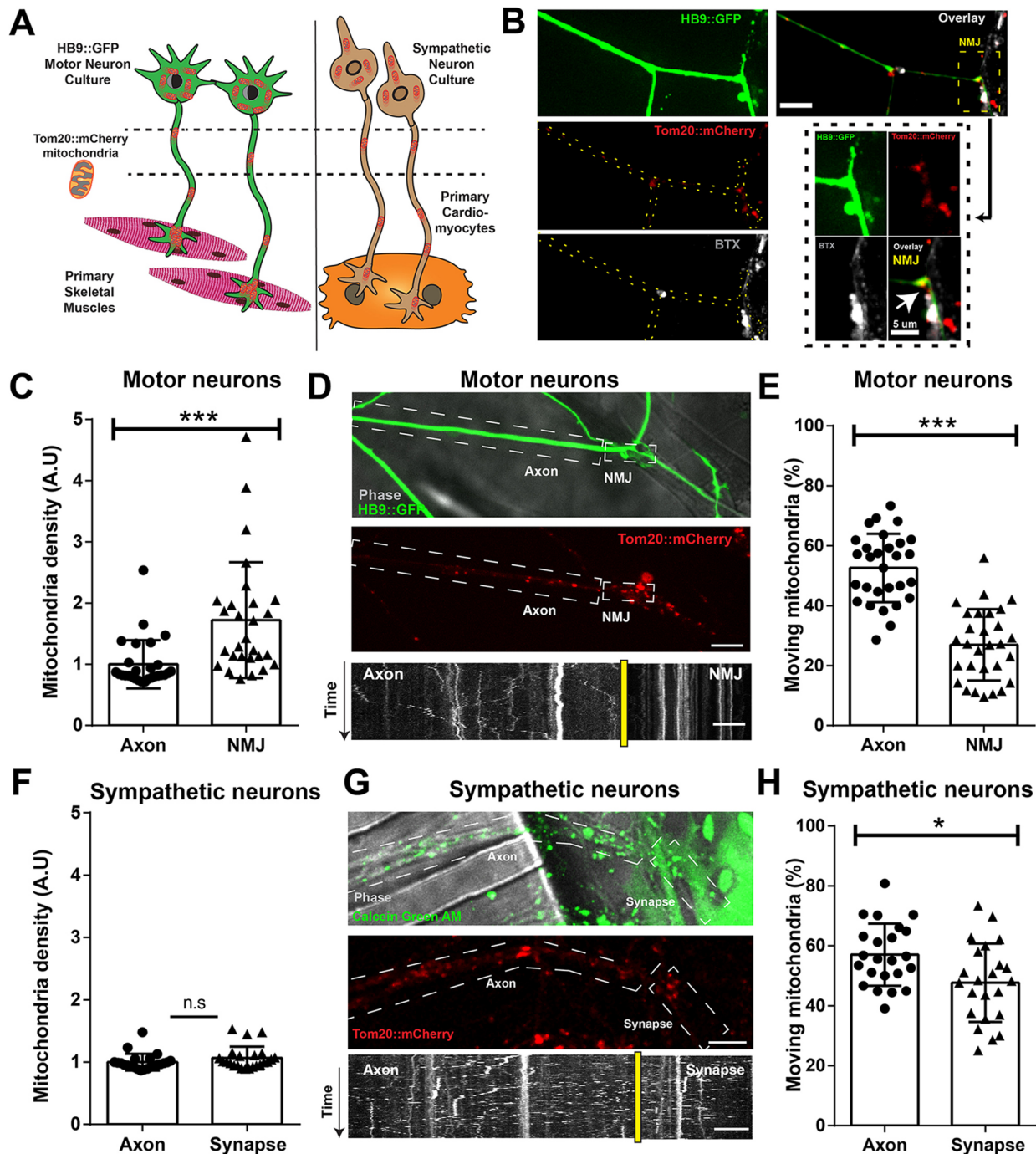### MN mitochondria accumulate in the NMJ in vitro

To further study the behavior of MN and SN mitochondria in co-culture, we decided to focus on mitochondria found in proximity to skeletal muscle and cardiomyocyte cells, namely, synaptic mitochondria. The MN and SN mitochondria were evaluated without a background of a myotube or a cardiomyocyte mitochondria, by infection of only the neuronal compartment (where dissociated MNs or SNs were plated) with Tom20::mCherry lentivirus (LV) (Fig. 3A). To determine whether mitochondria were localized to MN NMJs, we applied α-Bungarotoxin–ATTO-633, to mark post-synaptic acetyl choline receptors, and imaged co-culture synapses (Fig. 3B). Image analysis revealed a 72% increase in mitochondrial density in NMJ, compared with MN axons (Fig. 3C), thus suggesting a synaptic enrichment of mitochondria in this experimental setup. These novel results from in vitro NMJs are in accordance with previous observations of mitochondrial enrichment in NMJs in vivo (Misgeld et al., 2007). Next, we decided to image mitochondrial transport in proximity to muscle cells (Fig. 3D). Transport analysis revealed a near 2-fold decrease in mitochondrial movement in NMJs (Fig. 3E), suggesting that NMJ formation

actively leads to the docking of mitochondria. To validate that this is a unique MN quality, we conducted similar experiments in a SN–cardiomyocyte co-culture, which revealed no mitochondrial enrichment in sympathetic synapses (Fig. 3F). Furthermore, we imaged SN mitochondrial transport in a similar manner (Fig. 3G), which revealed a slight decrease in transport in SN–cardiomyocyte synapses (Fig. 3H). This might indicate that mitochondria are also halted in sympathetic synapses, but the higher rate of retrograde transport in SNs (Fig. 2) prevents efficient mitochondrial accumulation. Taken together, this suggests that NMJ formation leads to the accumulation of mitochondria only in the NMJ, a process not found in the SN–cardiomyocyte synapse.

NMJ ATP production is highly dependent on mitochondria

Mitochondria serve many critical purposes in cellular and neuronal biology, including ATP generation through oxidative phosphorylation. Unlike other cell types, which have a certain metabolic endurance, MNs are known to heavily depend on oxidative phosphorylation to produce ATP owing to their high metabolic needs (Vandoorne et al., 2018). Surprisingly, despite the importance of mitochondria for neurons and their high ATP demand, recent evidence suggests that many key neuronal processes, such as axonal transport (Zala et al., 2013) and synaptic vesicle release (Ashrafi et al., 2017) depend on glycolytic ATP. Since the NMJ is a unique and specialized synapse, we hypothesized that ATP generation in NMJ might have a stronger dependency on mitochondria than other synapses tested in the past, mostly CNS synapses, which seem to depend heavily on glycolytic ATP (Ashrafi and Ryan, 2017). To this end, we co-cultured MN and muscle cells and infected neurons with adeno-associated virus (AAV) coding an ATP FRET sensor, Ateam 1.03 (Imamura et al., 2009). The Ateam probe contains two fluorophores, CFP and Venus, in a distinct conformation. By bleaching the Venus fluorophore, we can measure the amount of ATP, calculated as increase in fluorescence of CFP channel or FRET efficiency (Fig. 4A) as previously described (Shulman et al., 2015; Gazit et al., 2016; Styr et al., 2019). Since Ateam proteins are fused to synaptophysin1-containing vesicles, they were enriched in neuronal synapses of our dissociated co-cultured MFC platform (Fig. 4B), and thus allowed us to visualize ATP changes in the pre-synapse compartment. First, we verified that ATP levels were stable after changing medium (Fig. 4C). Next, to determine the importance of mitochondria to ATP generated in the NMJ, we applied 5 μM oligomycin, a mitochondrial ATP synthase inhibitor, for 30 min to block oxidative phosphorylation. This led to a 25% decrease in ATP (Fig. 4C), highlighting the important role mitochondria play in generating ATP in the NMJ. Surprisingly, when we tested the minimum ATP signal found after addition of 5 μM oligomycin together with 25 mM of the glycolysis inhibitor 2-deoxy-glucose, there was a 30% decrease (Fig. 4C), which was not significantly different from the decrease caused by oligomycin alone. A similar experiment was conducted in the SN–cardiomyocyte system (Fig. 4D). The SN synapse ATP level was not significantly affected by medium exchange (Fig. 4C), but there was a 19% decrease in synaptic ATP following oligomycin treatment (Fig. 4E). However, the minimum ATP signal found after combining oligomycin and 2-deoxy-glucose was reduced by 39%, a further reduction of 20%. Taken together, this suggests that generation of ATP in MN NMJ is mostly derived from mitochondrial respiration, whereas glycolytic ATP plays a stronger role in other synapses such as the SN–cardiomyocyte synapse. This highlights the key contribution of MN mitochondrial localization at the NMJ to the ATP generation of this specialized synapse.

Fig. 3. Mitochondria accumulate in MN NMJs. (A) Schematic experimental setup of dissociated HB9::GFP MNs with skeletal muscles or dissociated SNs with cardiomyocytes in MFC. Mitochondria were marked through Tom20::mCherry LV infection. (B) *In vitro* NMJ, with HB9::GFP (green) marking the pre-synaptic MN, Bungarotoxin (BTX, white) showing post-synaptic acetyl choline receptor and Tom20::mCherry (red) showing mitochondria. The dotted yellow line denotes the axon and NMJ. Scale bar: 10 µm. The NMJ magnification on the bottom right shows pre-synaptic mitochondria accumulation. Scale bar: 5 µm. (C) Quantification of mitochondrial density in the axonal region compared to the NMJ (where the MN overlaps muscles). *n*=28 images analyzed, each image with at least one NMJ. ***$P<0.001$, Mann–Whitney test. (D) Phase (gray) image showing muscle overlapped by an HB9::GFP (green) MN, infected with Tom20::mCherry (red) marking mitochondria. The dashed white line indicates separation of the NMJ and axonal mitochondria. The kymograph displays Tom20::mCherry mitochondrial transport. The time of kymograph was 300 s. Scale bars: 10 µm. (E) Quantification of mitochondrial transport in NMJ segment compared with axonal segment. *n*=29 images were analyzed, each image with at least one NMJ. ***$P<0.001$, unpaired *t*-test. (F) Mitochondrial density quantification of the SN synapse region (an SN overlapping cardiomyocytes) compared with that in the axonal area. *n*=23 images analyzed, each image with at least one synapse. Mann–Whitney test. (G) Phase (gray) image showing a cardiomyocyte overlapped by an SN infected with Tom20::mCherry (red, marking neuronal mitochondria). Both the cardiomyocyte and SN are marked with Calcein-AM dye (green) to help identify cell localization. Dotted white line indicates SN separation between the cardiomyocyte-overlapping portion (synapse) and axonal mitochondria. The kymograph displays transport of Tom20::mCherry mitochondria. The time of kymograph was 300 s. Scale bars: 10 µm. (H) Quantification of mitochondrial transport in SN synapse segment compared with axonal segment. *n*=23 images were analyzed, each image with at least one synapse. *$P<0.05$, unpaired *t*-test. Each graph contains at least three independent biological repeats. Data represent mean±s.d. A.U., arbitrary units.
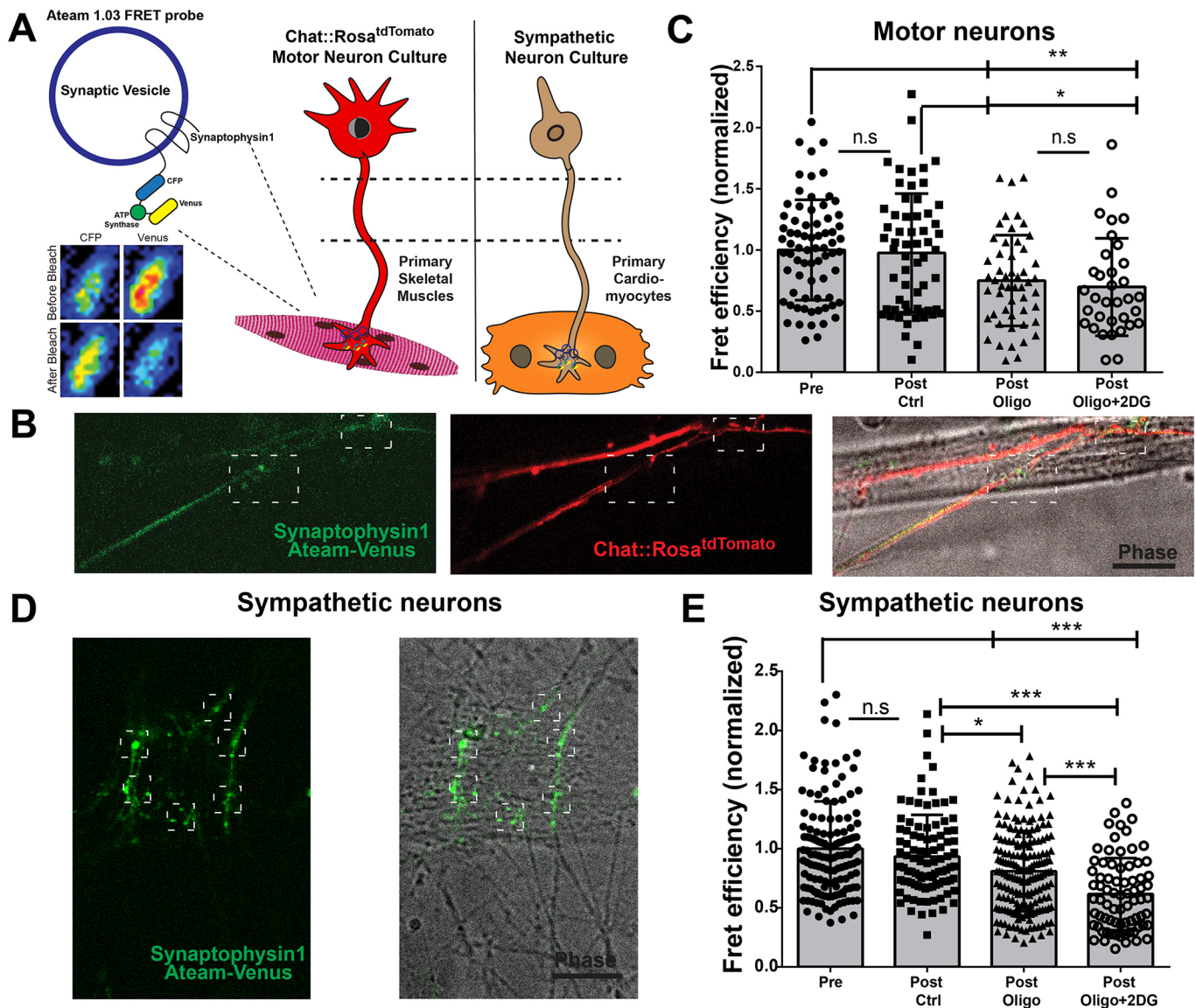
Fig. 4. MN NMJ but not SN synapse ATP is more sensitive to mitochondrial inhibition. (A) Schematic representation of ChAT::Rosa[tdTomato] MN–skeletal muscle or SN–cardiomyocyte co-culture, infected with Synaptophysin1 Ateam1.03 AAV to measure synaptic ATP. The FRET efficiency was calculated as the increase in CFP signal after photobleaching of the Venus signal puncta. (B) Ateam1.03 puncta (green) localized to a ChAT::Rosa[tdTomato] MN axon (red) specifically where the MN overlapped skeletal muscle (gray), and thus accumulated in the NMJ. Scale bar: 10 µm. (C) Ateam1.03 FRET efficiency after medium exchange (control), oligomycin (mitochondrial inhibitor) treatment and oligomycin+2-DG (glycolysis inhibitor) treatments. $n=72$ NMJ for pre-condition, $n=60$ for post control, $n=52$ for post oligomycin, $n=34$ for post oligomycin+2DG. **$P<0.01$, *$P<0.05$, one-way ANOVA with Holm–Sidak post-hoc test. (D) Ateam 1.03 puncta (green) localized to SNs in specific regions where an SN overlapped a cardiomyocyte (gray), and thus accumulated in the synapse. Scale bar: 10 µm. (E) Ateam1.03 FRET efficiency after medium exchange (control), oligomycin (mitochondrial inhibitor) treatment and oligomycin+2-DG (glycolysis inhibitor) treatments. $n=136$ puncta for pre-condition, $n=98$ for post control, $n=183$ for post oligomycin, $n=75$ for post oligomycin+2DG. ***$P<0.001$, **$P<0.01$, *$P<0.05$, one-way ANOVA with Holm–Sidak post-hoc test. Each graph contains at least three independent biological repeats. Data represent mean±s.d.

In summary, we used our MFC co-culture platform to generate an NMJ *in vitro* system. The system provided a simplified method to test mitochondrial localization and transport in the NMJ. Our data suggest that accumulation of mitochondria in the NMJ is possibly important for MN function in a healthy state. Future studies should determine whether this new finding could be relevant for the elucidation of the specific MN vulnerability occurring in MN diseases.

MATERIALS AND METHODS
Animals
HB9::GFP (stock no. 005029) mice were originally obtained from Jackson Laboratories (Bar Harbor, ME). The colony was maintained

by breeding with ICR mice (Jackson Laboratories). B6;129S6-Chat[tm2(cre)Lowl]/J (stock no. 006410) and B6;129S6Gt(ROSA) 26Sor[tm14(CAG−tdTomato)Hze]/J (stock no. 007908) mice were originally obtained from Jackson Laboratories, and were cross bred in the Tel-Aviv SPF animal unit to yield homozygous ChAT::Rosa[tdTomato] mice. The ChAT::Rosa[tdTomato] colony was maintained by in-breeding males and females from the colony. C57BL/6J mice were originally obtained from Jackson Laboratories as WT of the SOD1[G93A] (Stock No: 002726) mouse strain. Mice were genotyped via PCR (KAPA Bio systems, Wilmington, MA). DNA samples were generated from mouse ear or tail.

Animal experiments were performed under the supervision and approval of the Tel-Aviv University Committee for Animal Ethics.

Microfluidic chamber preparation

PDMS (Dow Corning Corp., Midland, MI) MFCs were designed and casted as previously described (Ionescu et al., 2016). For axonal transport and muscle contraction essays, three 7 mm wells were punched, and small 'caves' were further carved in the proximal compartment to enable SC explants or superior cervical ganglions to anchor and enter the growth channels. For the viral infection experiments (Figs 3 and 4), a dissociated MN culture was needed, and two 6 mm wells were punched instead of the 7 mm ones in either compartment, as described in Gershoni-Emek et al. (2018).

MFCs were cleaned first with adhesive tape to remove dirt and then soaked in 70% ethanol for 15 min, after which they were dried, and UV irradiated for 10 min. MFCs were then attached to a 35 or 50 mm FluoroDish glass-bottom dish (WPI) for dissociated MN culture or ventral SC explants, respectively.

For SC explants or MN only culture (as in Fig. 2A), both compartments were coated with 1.5 ng/ml polyornithine (Sigma-Aldrich, St Louis, MO) in PBS and left overnight, followed by overnight incubation with laminin (Sigma-Aldrich), at a ratio of 1:333 in deionized distilled water (DDW). For SN only (as in Fig. 2B) plating, both compartments were coated with 10 μg/ml poly-D-lysine (Sigma-Aldrich) in PBS and left overnight, and then replaced with laminin, at a ratio of 1:333 in DDW. For skeletal muscle or cardiomyocyte plating in a co-culture setting, only the proximal compartment was coated with polyornithine (for MN) or poly-D-lysine (for SN) overnight, and replaced with laminin at a ratio of 1:333 in DDW. The distal compartment was coated with Matrigel (BD Biosciences, San Jose, CA), diluted 1:50 in DMEM (Biological Industries, Beit-Haemek, Israel) containing 2.5% L-penicillin-Streptomycin-Nystatin (PSN; Biological Industries) overnight, and then replaced with laminin at a ratio of 1:100 in PBS.

Fluorescence microscopy and image analysis

All confocal images (except for Fig. 4) were captured using a Nikon Ti microscope equipped with a Yokogawa CSU X-1 spinning disc and an Andor iXon897 EMCCD camera controlled by Andor IQ3 software. Phase-contrast movies of muscle contraction were acquired using the same microscope in wide-field mode and images were captured with an Andor Neo sCMOS camera.

For Fig. 4 (Ateam 1.03 FRET experiments), confocal images were captured using an Olympus inverted microscope with a Yokogawa CSU X-1 spinning disc and an Andor iXon897 EMCCD camera controlled by Andor IQ3 software.

All live-imaging assays were performed at 37°C and in a 5% CO_2 controlled and humidified environment.

MN-skeletal muscle co-culture

Primary muscle culture and co-culturing procedures were performed as previously described (Ionescu et al., 2016). Briefly, C57BL/6J adult female mice were euthanized at the age of 60 days [postnatal day (P)60]. Gastrocnemius muscles were excised and treated with 2 mg/ml collagenase-I (Sigma-Aldrich) for 3 h. Muscles were then dissociated into single fibers and were collected into pre-coated Matrigel dishes for a 3-day incubation in a Bioamf-2 (Biological Industries) medium with 1% PSN. On the fourth, fifth and sixth days, cultures underwent pre-plating for isolation of a pure, fibroblast-free, myoblast culture. Next, 100,000 myoblasts were plated in the distal compartment of a pre-coated MFC. Cultures were grown and allowed to differentiate for another 7 days prior to the addition of a SC explant to the proximal compartment. For dissociated MN–skeletal muscle co-culture, 50,000 myoblasts were plated in the distal compartment 3 days prior to the addition of MN to the proximal compartment. Bioamf medium was applied to the distal compartment and refreshed every second day.

For SC explant co-culture, ventral SCs were dissected from embryonic day (E)12.5 embryos and plated in the proximal channel of the muscle containing MFC. On the same day, Bioamf-2 medium for muscles and SCEX medium [neurobasal medium (Gibco, Thermo Fisher Scientific, Waltham, MA), 1% glutamax (Gibco) and 1% penicillin-streptomycin], supplemented with 25 ng/ml BDNF (Alomone Labs, Jerusalem, Israel) for SC explants, was added to the proximal compartment. After 3 DIV, medium

in both compartments was replaced with SCEX medium with no supplements. Medium was refreshed every second day.

For dissociated MN co-culture, primary MNs were cultured from ventral SCs of E12.5 mouse embryos as previously described (Camu and Henderson, 1994; Kalmar and Greensmith, 2009). Briefly, SCs were excised, trypsinized and triturated. Supernatant was collected and centrifuged through a BSA cushion. The pellet was resuspended and centrifuged through an Optiprep gradient [10.4% Optiprep (Sigma-Aldrich), 10 mM Tricine (Sigma-Aldrich), 4% glucose] for 20 min at 760 g with the brake turned off. Next, the cells were collected from the interphase, washed once in complete medium, and then plated in a coated MFC proximal compartment at a density of 150,000 MNs per chamber. Cells were maintained in Complete neurobasal medium (Gibco) containing B27 (Thermo Fisher Scientific), 10% (v/v) horse serum (Thermo Fisher Scientific), 25 μM β-mercaptoethanol, 1% penicillin-streptomycin and 1% Glutamax, supplemented with 1 ng/ml GDNF, 0.5 ng/ml CNTF, and 25 ng/ml BDNF (all from Alomone Labs). To remove glial cells, MNs were treated with 1 μM ARA-C (Sigma-Aldrich) from 1 to 3 DIV. At 3 DIV, the supplement concentrations in the MN medium were lowered to 1 ng/ml BDNF, to create a gradient of muscle NTF, with no exogenous NTF, therefore increasing MNs crossing towards the distal muscle side.

SN–cardiomyocyte co-culture

For SN explant co-culture, superior cervical ganglions were dissected from P1 ICR mouse pups [based on a previously published protocol (Jackson and Tourtellotte, 2014)] and inserted into caves in the proximal compartment of the MFC. The SNs were grown in SCEX medium supplemented with 62.5 ng/ml NGF (Alomone) and replaced every second day.

For dissociated SN co-culture, superior cervical ganglions were dissected from postnatal day 1 (P1) ICR mouse pups and digested with 5 mg/ml Collagenase-I (Sigma-Aldrich) in L15 for 20 min at 37°C, followed by further digestion with Trypsin EDTA solution B (Biological Industries) for 20 min at 37°C. Trypsin was blocked by L15 with 10% fetal calf serum (Thermo Fisher), centrifuged and triturated 20 times and plated in a coated MFC proximal compartment at a density of 25,000 SNs per chamber, all in SCEX medium supplemented with 125 ng/ml NGF that was refreshed every second day. To remove glial cells, SNs were treated with 1 μM ARA-C (Sigma-Aldrich) from 1 to 3 DIV.

Primary cardiomyocytes were cultured as previously described (Ehler et al., 2013). Briefly, 5-10 hearts were dissected from postnatal day 0 (P0) ICR mouse pups into HBSS (Thermo Fisher) supplemented with 20 mM BDM (Sigma-Aldrich). Hearts were cleaned to remove blood vessels and blood, and then transferred into 250 μl drops of isolation medium (85% HBSS, 20 mM BDM, 5% Trypsin B; Biological Industries) and cut with scissors into small pieces. The minced hearts were transferred to 10 ml of isolation medium and incubated for 15 min at 37°C. Afterwards, the medium was gently replaced without touching the heart fragments with digestion medium (90% L-15, 10% BDM, 1.42 mg/ml collagenase type 2; Worthington, Columbus, OH) and was incubated for 30 min at 37°C. Next, the hearts were washed through a 40 μm pore cell strainer and rinsed with 10 ml L-15 (Thermo Fisher Scientific) to remove debris and aggregates. The flow-through cells were centrifuged for 10 min at 100 g and resuspended in complete cardiac medium [39% DMEM, 40% F-10 (Thermo Fisher Scientific), 10% horse serum, and 10% fetal calf serum (Thermo Fisher Scientific), and 1% penicillin-streptomycin]. The resuspended cells were then pre-plated on a plastic 10 cm plate for 2 h at 37°C to remove fibroblasts. After incubation, the non-adherent cells were collected, centrifuged (400 g for 5 min) and 25,000 cardiomyocytes per chamber were inserted into the distal compartment of the MFC. The cells were plated in myocyte growth medium (Promo Cell, Heidelberg, Germany). Medium was refreshed every second day. To aid SN crossing, from DIV 1 the myocyte medium was also supplemented with 125 ng/ml of NGF.

Immunofluorescence staining

In vitro NMJs from co-cultures of MN–skeletal muscle, SN–cardiomyocyte or muscle only cultures were stained as previously described (Gershoni-Emek et al., 2018). Briefly, co-cultures were plated in a glass-bottom plate and fixed after 7 DIV with 4% PFA for 20 min. Next, α-Bungarotoxin-633 1:100 (Alomone) was used to mark post-synaptic acetylcholine receptors in the MN

NMJ prior to permeabilization. Permeabilization for 30 min was performed using 0.1% Triton X-100 in PBS with blocking solution [1 mg/ml BSA (Amresco, Radnor, PA) and 10% goat serum (Enco, Petach Tikvah, Israel)]. Cultures were then blocked for 30 min in blocking solution (no Triton X-100 detergent) and labeled overnight with primary antibodies: rabbit anti-Synapsin-I, 1:1000 (Abcam, ab1543p); chicken anti-NFH, 1:500 (Abcam, ab72996); mouse anti-α-actinin, 1:100 (Santa Cruz Biotechnology, sc-17829), and rabbit anti-RYR, 1:400 (Milipore, AB9078). Next, a 2-h incubation with secondary antibodies was performed. The secondary antibodies used were Alexa-Fluor-405-conjugated anti-chicken-Ig, 1:500 (abcam, ab175675); Alexa-Fluor-488-conjugated anti-rabbit-Ig, 1:1000 (Invitrogen, A11034), and Alexa-Fluor-594-conjugated anti-mouse-Ig, 1:500 (Invitrogen, A11032).

The stained cultures were imaged in a Nikon confocal microscope using a 60× oil objective.

Skeletal muscle and cardiomyocyte contraction analysis and TTX experiments

Co-cultures were grown for 7 days post-neuron plating. Then, the contractile activity of muscles, which overlapped by at least one axon in the distal compartment of the MFC, was observed by imaging for 30 s, 1000 frame movies using 20× magnification using an Andor Neo sCMOS camera. Afterwards, medium in the neuronal proximal compartment was replaced with fresh medium containing 1 μM TTX to inhibit MN firing. Movies were imaged again at the same field of view as the pre-treatment condition to observe the same muscles prior to TTX treatment.

For skeletal muscle analysis, the muscles were counted as either contracting or non-contracting, based on their activity. The number of contracting muscles per movie was divided by the total number of innervated muscles in the field of view, yielding the percentage of contracting myotubes.

For cardiomyocyte analysis, each cardiomyocyte contraction was counted before and after TTX treatment. The analysis was done by generating intensity over time plots using the ImageJ Time Series Analyzer plugin, followed by manual counting of graph peaks as in Ionescu et al. (2016).

Mitochondrial axonal transport analysis

MNs or SNs were grown for 7 DIV with or without the presence of skeletal muscle or cardiomyocytes, respectively. On the seventh day, the cultures were stained in all compartments using 100 nM of Mitotracker Deep-Red FM (Molecular Probes, M22426) for 30 min at 37°C, followed by three washes with warm medium. For live imaging, movies of 100 frames were collected in 3 s intervals from the distal part of the MFC grooves using a 60× oil objective.

For MN and SN cultures treated with muscle or cardiomyocyte conditioned medium, MN and SN explants were grown for 7 DIV. At DIV 7, medium was exchanged in both compartments to starvation medium without neurotrophic factors and B27 [neurobasal medium (Gibco), 1% glutamax (Gibco), 1% penicillin-streptomycin] for overnight incubation. The following day, the cultures were stained as above, and imaged. After imaging, only the medium in the distal compartment was replaced with fresh muscle (for MN) or cardiomyocyte (for SN) conditioned medium for 3 h of incubation, followed by a second round of imaging. For conditioned medium application, skeletal muscles (for MN) or cardiomyocytes were plated at the same day as the neuronal culture in a Matrigel-coated 24-well plate at a density of 250,000 muscles or 100,000 cardiomyocytes per well. After 7 DIV, muscle or cardiomyocyte medium was exchanged to starvation medium for overnight incubation at a volume of 300 μl per well. The medium was collected the following day and immediately applied onto the MN or SN axonal compartment.

For co-culture over time experiments, the cultures were stained on the fifth, seventh and ninth day in a similar manner. All analyzed MFCs were stained and imaged in all three time points.

Live axonal transport movies were analyzed using the Kymo ToolBox ImageJ plugin to generate and analyze kymographs (Gershoni-Emek et al., 2018). The moving directionality of mitochondria was determined for each individual mitochondrial track, and the total particle directionality was calculated for each axon. Particles moving in the anterograde (moving right in the kymograph) or retrograde (moving left) direction were classified after moving more than 10 μm in the specific direction. Rotating particles or particles moving for less than 10 μm were defined as non-moving.

Quantification of mitochondrial localization and transport in MN NMJs and SN synapses

To quantify the number of MN and SN mitochondria in the synapse, and to avoid the muscle and cardiomyocyte mitochondrial background, co-cultures of skeletal muscles and dissociated HB9::GFP-expressing MNs, or cardiomyocytes and dissociated SNs, were infected with LV encoding Tom20::mCherry. Infection was performed at 2 h post plating of dissociated MNs in the MFC proximal compartment. LVs were applied only to the proximal compartment to avoid muscle infection.

To quantify the number of MN mitochondria in the NMJ colocalization, at 9 DIV α-Bungarotoxin-633 (Alomone) 1:100 was applied to stain the NMJ post-synaptic site, by incubation for 15 min at 37°C. Multi-stack images of the co-culture were generated using a 60× oil objective. To quantify MN mitochondria transport in the NMJ, a similar protocol was carried out without bungarotoxin application, because this starts internalizing after 30–60 min and loses specific signal. Instead, the NMJ was determined as a MN clearly overlapping a contracting skeletal muscle. Movies of 100 frames (5 min) were taken. Because of muscle thickness, multi-stack images were taken for each time frame. For SNs mitochondria synaptic colocalization and transport, similar Tom20::mCherry LV infection was performed. However, as cardiomyocytes are flatter and harder to see in phase-contrast images, CellTrace™ Calcein Green dye (Thermo Fisher Scientific, C34852) was applied to the distal compartment at a concentration of 2.5 μg/ml to help distinguish SN–cardiomyocyte overlapping sites. Only contracting cardiomyocytes were imaged. Similarly, movies of 100 frames (5 min) were taken with multi-stack images for each time frame.

The images for colocalization analysis were analyzed using the ImageJ measure tool. For MNs, the HB9::GFP channel was used to mark the axonal processes, which were divided into NMJ and axonal portions (defined by axons colocalized with a BTX channel for mitochondria density quantification or by muscle overlap in the transport essay). For SN–cardiomyocytes, co-cultures were visualized using Calcein Green dye, and synapses were determined were SNs that clearly overlapped a contracting cardiomyocyte. For both MNs and SNs, the average mitochondrial density was calculated as the average Tom20::mCherry intensity in the synapse segment normalized to the intensity in the axonal segment.

The transport movies were analyzed using the Kymo ToolBox ImageJ plugin. MN axons and NMJs, or SN axons and synapses were determined as described above. A separate kymograph was generated for the synapse segment and the axon segment. Each individual mitochondria spotted in the kymograph was counted as moving or non-moving. Because the NMJ or SN synapse segments could be very short (down to 20 μm), even slight movements of 5 μm were counted as moving mitochondria, yielding a higher movement ratio for MNs than observed in the regular axonal transport essay (Fig. 2; Figs S2 and S3). The movement proportions were calculated for the total synaptic or axonal segments of each image (and not for each axon like in the Fig. 2 axonal transport analysis).

Quantification of ATP in NMJs using Ateam 1.03

To quantify synaptic ATP in the NMJs or SN synapses, co-cultures of skeletal muscles and dissociated Chat::Rosa^{tdTomato} MNs or cardiomyocytes and dissociated SNs were infected 2 h post-plating with AAV encoding synaptophysin1-fused Ateam 1.03 (Shulman et al., 2015). Neurons expressing the virus were detected, and their NMJ/SN synapse was determined from the overlap of the neuron and the muscle in phase-constant images (Fig. 4C). Only neurons overlapping contracting muscles/cardiomyocytes were chosen for imaging. Plates were divided into three groups: the control condition, oligomycin and oligomycin+2-deoxy-glucose (2DG). Each plate was imaged before and 30 min after drug or fresh medium application (for the control condition). In the oligomycin+2DG condition the medium was free of glucose, pyruvate or glutamine supplementation to prevent activation of alternative ATP generation pathways.

FRET efficiency was determined as previously described (Shulman et al., 2015; Gazit et al., 2016; Styr et al., 2019). Ateam 1.03 CFP donor was excited using a 445 nm laser and its emission was measured at 460–485 nm before and after Venus acceptor photobleaching. Acceptors were excited using a 514 nm laser and emission was measured at 530–560 nm.

Photobleaching of the Venus channel was achieved using the Andor Frappa tool, by single-point marking of individual synaptophysin1-positive puncta and multi-point excitation with 100% laser power at a 514 nm wavelength.

For image analysis, the intensity of every synaptic puncta was calculated under four conditions: for the CFP and Venus channels, before and after photobleaching. For every puncta, the average intensity was measured under all four conditions and the background noise was reduced. FRET efficiency was calculated as (CFP after bleach-CFP before bleach)/CFP after bleach. Synapses that exhibited less than a 65% reduction in the Venus signal after bleaching were excluded to rule out random changes in intensity.

Lentivirus and adeno-associated-virus production and infection

LVs and AAVs were produced in HEK cells. LV production was aided using a second-generation packaging system with Gag-Pol and VSVG helpers, and AAVs with pDP1 and pDP2 helpers. HEK cells were grown on a 60-mm dish at 70 to 80% confluence and then transfected using 10 µg of LV/AAV vector and 10 µg of helper plasmids. Plasmids were placed in a calcium phosphate transfection mix (25 mM Hepes, 5 mM KCl, 140 mM NaCl, and 0.75 mM Na2PO4 with 125 mM CaCl^2) before their addition to cells, in a volume of 0.5 ml per plate. Culture supernatants were harvested 2 days after transfection. LVs were concentrated 10-fold by using the PEG virus precipitation kit (Abcam). LVs were kept at −80°C until use and AAVs at 4°C. Viral infection was performed using 5–10 µl of LV or AAV per MFC, at 2 h post MN or SN plating.

Statistical analysis

All statistical analyses were performed using GraphPad Prism v6.0. Values are presented with s.d. for pooled analysis of individual values where n represents the number of axons, muscles, synapses or images. This was done as there was high variability in the number of infected neurons per chamber. Values are presented with s.e.m. for grouped analysis, where n represents the number of MFCs analyzed. For grouped analysis, each MFC was counted as a biological repeat and contained at least eight imaged axons (relevant for Fig. 2, Figs S2 and S3). For two-group analysis, Student's t-test or the Mann–Whitney test were used, as determined by a normality test. For multiple comparisons, one-way or two-way ANOVA was used with a Holm–Sidak post-hoc test. All experiments were repeated at least three times, and significance was set at $P<0.05$.

References
Ashrafi, G. and Ryan, T. A. (2017). Glucose metabolism in nerve terminals. Curr. Opin. Neurobiol. 45, 156-161. doi:10.1016/j.conb.2017.03.007
Ashrafi, G., Wu, Z., Farrell, R. J. and Ryan, T. A. (2017). GLUT4 mobilization supports energetic demands of active synapses. Neuron 93, 606-615.e3. doi:10.1016/j.neuron.2016.12.020
Bilsland, L. G., Sahai, E., Kelly, G., Golding, M., Greensmith, L. and Schiavo, G. (2010). Deficits in axonal transport precede ALS symptoms in vivo. Proc. Natl. Acad. Sci. USA 107, 20523-20528. doi:10.1073/pnas.1006869107

Burke, R. E. and Tsairis, P. (1973). Anatomy and innervation ratios in motor units of cat gastrocnemius. J. Physiol. 234, 749-765. doi:10.1113/jphysiol.1973.sp010370
Burke, R. E., Strick, P. L., Kanda, K., Kim, C. C. and Walmsley, B. (1977). Anatomy of medial gastrocnemius and soleus motor nuclei in cat spinal cord. J. Neurophysiol. 40, 667-680. Available at: http://e.guigon.free.fr/rsc/article/BurkeREEtAl77.pdf (Accessed: 12 May 2019). doi:10.1152/jn.1977.40.3.667
Camu, W. and Henderson, C. E. (1994). Rapid purification of embryonic rat motoneurons: an in vitro model for studying MND/ALS pathogenesis. J. Neurol. Sci. 124 Suppl., 73-74. (Accessed: 13 May 2019). doi:10.1016/0022-510X(94)90185-6
Catala, M. and Kubis, N. (2013). Gross anatomy and development of the peripheral nervous system. Handb. Clin. Neurol. 115, 29-41. doi:10.1016/B978-0-444-52902-2.00003-5
Collard, J.-F., Côté, F. and Julien, J.-P. (1995). Defective axonal transport in a transgenic mouse model of amyotrophic lateral sclerosis. Nature 375, 61-64. doi:10.1038/375061a0
Conforti, L., Tohse, N. and Sperelakis, N. (1991). Influence of sympathetic innervation on the membrane electrical properties of neonatal rat cardiomyocytes in culture. J. Dev. Physiol. 15, 237-246. (Accessed: 13 May 2019).
Cserép, C., Pósfai, B., Schwarcz, A. D. and Dénes, Á. (2018). Mitochondrial ultrastructure is coupled to synaptic performance at axonal release sites. eNeuro 5, ENEURO.0390-17.2018. doi:10.1523/ENEURO.0390-17.2018
Devine, M. J. and Kittler, J. T. (2018). Mitochondria at the neuronal presynapse in health and disease. Nat. Rev. Neurosci. 19, 63-80. doi:10.1038/nrn.2017.170
Ehler, E., Moore-Morris, T. and Lange, S. (2013). Isolation and culture of neonatal mouse cardiomyocytes. J. Vis. Exp. 79, e50154. doi:10.3791/50154
Fecher, C., Trovò, L., Müller, S. A., Snaidero, N., Wettmarshausen, J., Heink, S., Ortiz, O., Wagner, I., Kühn, R., Hartmann, J. et al. (2019). Cell-type-specific profiling of brain mitochondria reveals functional and molecular diversity. Nat. Neurosci. 22, 1731-1742. doi:10.1038/s41593-019-0479-z
Gazit, N., Vertkin, I., Shapira, I., Helm, M., Slomowitz, E., Sheiba, M., Mor, Y., Rizzoli, S. and Slutsky, I. (2016). IGF-1 receptor differentially regulates spontaneous and evoked transmission via mitochondria at hippocampal synapses. Neuron 89, 583-597. doi:10.1016/j.neuron.2015.12.034
Gershoni-Emek, N., Altman, T., Ionescu, A., Costa, C. J., Gradus-Pery, T., Willis, D. E. and Perlson, E. (2018). Localization of RNAi machinery to axonal branch points and growth cones is facilitated by mitochondria and is disrupted in ALS. Front. Mol. Neurosci. 11, 311. doi:10.3389/fnmol.2018.00311
Gibbs, K. L., Kalmar, B., Rhymes, E. R., Fellows, A. D., Ahmed, M., Whiting, P., Davies, C. H., Greensmith, L. and Schiavo, G. (2018). Inhibiting p38 MAPK alpha rescues axonal retrograde transport defects in a mouse model of ALS. Cell Death Dis. 9, 596. doi:10.1038/s41419-018-0624-8
Gylys, K. H., Fein, J. A., Yang, F. and Cole, G. M. (2004). Enrichment of presynaptic and postsynaptic markers by size-based gating analysis of synaptosome preparations from rat and human cortex. Cytometry A 60, 90-96. doi:10.1002/cyto.a.20031
Hafezparast, M. (2003). Mutations in dynein link motor neuron degeneration to defects in retrograde transport. Science 300, 808-812. doi:10.1126/science.1083129
Harris, J. J., Jolivet, R. and Attwell, D. (2012). Synaptic energy use and supply. Neuron 75, 762-777. doi:10.1016/j.neuron.2012.08.019
Imamura, H., Huynh Nhat, K. P., Togawa, H., Saito, K., Iino, R., Kato-Yamada, Y., Nagai, T. and Noji, H. (2009). Visualization of ATP levels inside single living cells with fluorescence resonance energy transfer-based genetically encoded indicators. Proc. Natl. Acad. Sci. USA 106, 15651-15656. doi:10.1073/pnas.0904764106
Ionescu, A., Zahavi, E. E., Gradus, T., Ben-Yaakov, K. and Perlson, E. (2016). Compartmental microfluidic system for studying muscle–neuron communication and neuromuscular junction maintenance. Eur. J. Cell Biol. 95, 69-88. doi:10.1016/j.ejcb.2015.11.004
Jackson, M. and Tourtellotte, W. (2014). Neuron culture from mouse superior cervical ganglion. Bio-Protoc. 4, e1035. (Accessed: 13 May 2019). doi:10.21769/BioProtoc.1035
Jones, R. A., Harrison, C., Eaton, S. L., Llavero Hurtado, M., Graham, L. C., Alkhammash, L., Oladiran, O. A., Gale, A., Lamont, D. J., Simpson, H. et al. (2017). Cellular and molecular anatomy of the human neuromuscular junction. Cell Rep. 21, 2348-2356. doi:10.1016/j.celrep.2017.11.008
Kalmar, B. and Greensmith, L. (2009). Activation of the heat shock response in a primary cellular model of motoneuron neurodegeneration-evidence for neuroprotective and neurotoxic effects. Cell. Mol. Biol. Lett. 14, 319-335. doi:10.2478/s11658-009-0002-8
Lee, C. W. and Peng, H. B. (2006). Mitochondrial clustering at the vertebrate neuromuscular junction during presynaptic differentiation. J. Neurobiol. 66, 522-536. doi:10.1002/neu.20245
Magrané, J., Cortez, C., Gan, W. B. and Manfred, G. (2014). Abnormal mitochondrial transport and morphology are common pathological denominators in SOD1 and TDP43 ALS mouse models. Hum. Mol. Genet. 23, 1413-1424. doi:10.1093/hmg/ddt528
Misgeld, T. and Schwarz, T. L. (2017). Mitostasis in neurons: maintaining mitochondria in an extended cellular architecture. Neuron 96, 651-666. doi:10.1016/j.neuron.2017.09.055

Misgeld, T., Kerschensteiner, M., Bareyre, F. M., Burgess, R. W. and Lichtman, J. W. (2007). Imaging axonal transport of mitochondria *in vivo*. *Nat. Methods* **4**, 559-561. doi:10.1038/nmeth1055

Münch, C., Sedlmeier, R., Meyer, T., Homberg, V., Sperfeld, A. D., Kurt, A., Prudlo, J., Peraus, G., Hanemann, C. O., Stumm, G. et al. (2004). Point mutations of the p150 subunit of dynactin (DCTN1) gene in ALS. *Neurology* **63**, 724-726. doi:10.1212/01.WNL.0000134608.83927.B1

Oh, Y., Cho, G.-S., Li, Z., Hong, I., Zhu, R., Kim, M.-J., Kim, Y. J., Tampakakis, E., Tung, L., Huganir, R. et al. (2016). Functional coupling with cardiac muscle promotes maturation of hPSC-derived sympathetic neurons. *Cell Stem Cell* **19**, 95-106. doi:10.1016/j.stem.2016.05.002

Piccione, E. A., Sletten, D. M., Staff, N. P. and Low, P. A. (2015). Autonomic system and amyotrophic lateral sclerosis. *Muscle Nerve* **51**, 676-679. doi:10.1002/mus.24457

Saab, A. S., Tzvetavona, I. D., Trevisiol, A., Baltan, S., Dibaj, P., Kusch, K., Möbius, W., Goetze, B., Jahn, H. M., Huang, W. et al. (2016). Oligodendroglial NMDA receptors regulate glucose import and axonal energy metabolism. *Neuron* **91**, 119-132. doi:10.1016/j.neuron.2016.05.016

Shepherd, G. M. G. and Harris, K. M. (1998). Three-dimensional structure and composition of CA3→CA1 axons in rat hippocampal slices: implications for presynaptic connectivity and compartmentalization. *J. Neurosci.* **18**, 8300-8310. doi:10.1523/JNEUROSCI.18-20-08300.1998

Shulman, Y., Stavsky, A., Fedorova, T., Mikulincer, D., Atias, M., Radinsky, I., Kahn, J., Slutsky, I. and Gitler, D. (2015). ATP binding to synapsin IIa regulates usage and clustering of vesicles in terminals of hippocampal neurons. *J. Neurosci.* **35**, 985-998. doi:10.1523/JNEUROSCI.0944-14.2015

Styr, B., gonen, N., Zarhin, D., Ruggiero, A., Atsmon, R., Gazit, N., Braun, G., Frere, S., Vertkin, I., Shapira, I. et al. (2019). Mitochondrial regulation of the hippocampal firing rate set point and seizure susceptibility. *Neuron* **102**, 1009-1024.e8. doi:10.1016/j.neuron.2019.03.045

Vandoorne, T., De Bock, K. and Van Den Bosch, L. (2018). Energy metabolism in ALS: an underappreciated opportunity? *Acta Neuropathol.* **135**, 489-509. doi:10.1007/s00401-018-1835-x

Zahavi, E. E., Ionescu, A., Gluska, S., Gradus, T., Ben-Yaakov, K. and Perlson, E. (2015). A compartmentalized microfluidic neuromuscular co-culture system reveals spatial aspects of GDNF functions. *J. Cell Sci.* **128**, 1241-1252. doi:10.1242/jcs.167544

Zala, D., Hinckelmann, M.-V., Yu, H., Lyra da Cunha, M. M., Liot, G., Cordelières, F. P., Marco, S. and Saudou, F. (2013). Vesicular glycolysis provides on-board energy for fast axonal transport. *Cell* **152**, 479-491. doi:10.1016/j.cell.2012.12.029